









# Preliminary Studies on CIMR Antenna Pattern Brightness Temperature Compensation

Marco Brogioni , *Member, IEEE*, Ada Vittoria Bosisio , *Member, IEEE*, Alessandro Lapini ,  
Giovanni Macelloni , *Senior Member, IEEE*, Giuseppe Addamo , *Member, IEEE*,  
Giuseppe Virone , *Senior Member, IEEE*, Walter Di Nicolantonio, Marco Grilli , and Oscar A. Peverini 

**Abstract**—Spaceborne microwave radiometry provides an essential contribution to monitoring the Earth with varying spatial resolution both related to the reflector dimension and the frequency of operation. The ESA’s Copernicus imaging microwave radiometer (CIMR) mission aims at collecting the geophysical observables at a spatial resolution ranging from 60 km in L band to 4 km in Ka band. This goal can be achieved by equipping CIMR with a large unfurlable mesh reflector antenna. A limitation of the antenna design is that the antenna pattern includes grating lobes that contaminate the scene measurement with contributions originated far from the nominal footprint. This effect introduces inaccuracies in brightness temperature measurements, particularly when facing radiometric discontinuities, e.g., near the coastlines and sea ice edges, which can be greater than the mission required maximum of 0.5 K. The aim of this article is to assess a technique which will be able to correct the effects of antenna pattern and obtain reliable  $T_B$  measurements. The analyzed simple technique is based on a regularized deconvolution of the antenna pattern to reconstruct the actual brightness temperatures. The technique was tested over a synthetic scenario that mimics both steep and smooth variations in spatial and thermal domains.

**Index Terms**—Antenna pattern correction (APC), Copernicus imaging microwave radiometer (CIMR), microwave radiometry, radiometric resolution.

## I. INTRODUCTION

SINCE the late ‘70s, microwave radiometry has established itself as one of the most powerful tools for monitoring the Earth’s surface and its atmosphere [1]–[5]. The geophysical parameters that have benefited most from this technique

include vegetation biomass, soil moisture, sea surface temperature (SST), total precipitable water, water vapor, snow water equivalent, sea ice concentration (SIC), etc. The main advantages of microwave radiometry with respect to other techniques are the sensitivity to the presence and state of water in the scene, the all-day availability, and the relative low noise in the measurements. The main drawback of spaceborne radiometry is the achievable spatial resolution that limits its applicability to a wider range of applications. Indeed, real aperture radiometers equipped with reflectors having diameter size about 1–2 m achieve a ground spatial resolution of tens of kms, depending on the frequency of the operation. As an example, the Advanced Microwave Scanning Radiometer 2 (AMSR2) launched by the Japan space agency-JAXA onboard their GCOM-W1 satellite in 2012 [6], is one of the most advanced spaceborne radiometers with a spatial resolution of 35 km × 62 km at C-band (6.925/7.3 GHz) and 7 km × 12 km at Ka-band (36.5 GHz). At L-band larger antennas must be used, as in the NASA’s SMAP mission having a reflector of 6 m and a ground resolution of 40 km [7] or ESA’s SMOS which uses interferometry for obtaining a similar ground resolution [8]. Also, those antennas have a relatively wide main beam causing a land/sea contamination that can extend for hundreds of kms from the coasts (see [9] for Aquarius). In these regions the radiometric data are not accurate and should be used with particular care.

The observation of the state of regional seas in the polar/Arctic area requires a finer resolution for monitoring the variations of characteristic parameters, such as the SIC, and for being able to operate close to the coasts. In that sense, the European Commission proposed an “an integrated European Union (EU) policy for the arctic.” In consideration of the sparse population and the lack of transport infrastructure and links in the Arctic region, this policy identifies spaceborne microwave radiometry as the most useful tool for forwarding the identified agenda.

The Copernicus imaging microwave radiometer (CIMR) aims at providing high-spatial resolution of both microwave imaging radiometry measurements and their derived products in the Arctic region. CIMR Mission is one of the six Copernicus high priority candidate missions, an Earth monitoring initiative led by the EU and carried out in partnership with the EU Member States and the European Space Agency. The primary objectives of CIMR are the estimates in nonprecipitating atmosphere of the SIC and sea ice extent with a spatial resolution  $\leq 5$  km and an uncertainty of  $\leq 5\%$ , and of the SST with a spatial resolution  $\leq 15$

Manuscript received May 29, 2021; revised September 14, 2021 and October 22, 2021; accepted October 26, 2021. Date of publication November 4, 2021; date of current version December 23, 2021. This work was supported by OHB Italia as Instrument Prime, in the framework of the Phase A/B1 study of the CIMR mission, a program of and funded by the European Space Agency with the industrial leadership of Thales Alenia Space Italia. (*Corresponding author: Ada Vittoria Bosisio.*)

Marco Brogioni, Alessandro Lapini, and Giovanni Macelloni are with the Istituto di Fisica Applicata Nello Carrara, National Research Council of Italy, Sesto Fiorentino 50019, Italy (e-mail: m.brogioni@ifac.cnr.it; a.lapini@ifac.cnr.it; g.macelloni@ifac.cnr.it).

Ada Vittoria Bosisio, Giuseppe Addamo, Giuseppe Virone, and Oscar A. Peverini are with the National Research Council of Italy, Istituto di Elettronica ed Ingegneria dell’Informazione e delle Telecomunicazioni, Torino 10129, Italy (e-mail: adavittoria.bosisio@ieiit.cnr.it; giuseppe.addamo@ieiit.cnr.it; giuseppe.virone@ieiit.cnr.it; oscar.peverini@ieiit.cnr.it).

Walter Di Nicolantonio and Marco Grilli are with the OHB Italia, Milano 20151, Italy (e-mail: walter.dinicolantonio@ohb-italia.it; marco.grilli@ohb-italia.it).

Digital Object Identifier 10.1109/JSTARS.2021.3124829

km and an uncertainty  $\leq 0.2$  K. Special attention is given to the polar regions with the request of subdaily revisit and “no hole at the pole” spatial coverage. These objectives imply high-accuracy measurements that translate into a required maximum brightness temperature ( $T_B$ ) error, i.e., radiometer noise and contamination error, in the presence of radiometric discontinuities, less than 0.5 K at a distance from the discontinuity equal to the spatial resolution [10].

These and other driving factors led to the definition of a conical scanning radiometer with a rotating antenna assembly (composed of a reflector and a feed cluster) operating from L to Ka band in dual polarization. To fulfill the required coverage and spatial resolution within the applicable mass and volume constraints, the baseline solution foresees a deployable mesh reflector with a diameter of about 7 m, whose major impairments are the gain reduction and the occurrence of grating lobe effects in the radiation pattern. This degradation in the antenna performances is more detrimental at higher frequencies and proper countermeasures have to be developed.

The mitigation of the effects of the radiation pattern of an actual antenna is a well-known issue in microwave satellite observations. Sidelobe contamination and cross-polarization coupling, if acquisitions occur in dual polarization, are the two main unwanted effects [11]. In early missions, the antenna pattern correction (APC) mainly aimed at quantifying the fraction of power coming from the sidelobes [12] to correct the antenna temperature measurements from contributions pertaining to different angular regions. The correction should be applied to each frequency channel to accommodate the antenna beam width [13].

Other approaches, as in [14] and [15], are focused on the effects due to the antenna pattern, or to its changes in space, not exactly known. The retrieval process that theoretically involves the solution of an integral equation is performed by means of a discretized formulation of the apparent temperature with the addition of a priori knowledge about the scenario temperature distribution to minimize the error in the inversion. In [16], the actual antenna pattern is synthesized through a user-specified function that weighs up the radiometric image of the scene in a similar way to the point spread function used in radio astronomy observations. Then, the numerical deconvolution is fast Fourier transform (FFT)-based that also improves the spatial resolution.

More recent spaceborne sensors like NASA SMAP, Aquarius, GMI and the US NRL Windsat use a different approach to perform the APC [17]. The radiometric measurement  $T_A$  is corrected for unwanted direct and reflected sources like the sun, the moon, and galaxies to single out the contribution of the Earth,  $T_{A\text{Earth}}$ . Then, a constant  $4 \times 4$  matrix ( $2 \times 2$  for GMI) derived from global simulations based on the prelaunch models of the antenna pattern is used to perform the APC that aims at correcting the antenna sidelobes, cross-coupling contributions, and main beam efficiency. The approach is detailed in the GMI ATBD [18]. The method for determining the APC coefficients assumes that the  $T_B$  is constant over the whole pattern if the boresight vector intersects the Earth surface. To this end, only scenarios far from land were used from the global simulations

given that near coastlines and other geographical interfaces there can be considerable contamination to the main lobe scene due to this latter seeing the ocean while its near-sidelobes see the land, which has a very different brightness temperature. As an example [18] suggests centering the swath over the Pacific and skip any observation whose boresight is closer than 100 km from land or ice. This kind of approach cannot be used for CIMR given that accurate  $T_B$  measurements close to any radiometric transitions (e.g., sea/land or sea/ice) are specifically required [10].

Moreover, unlike previous spaceborne radiometers, the CIMR antenna pattern is characterized, especially at its highest frequencies, by the presence of strong and numerous grating lobes which are able to collect a relevant part of energy (4% of the total) very far (i.e., 50 to 200 km at Ka band) from the main beam.

In this article, the authors explore the applicability of a simple APC technique for reducing the artefacts introduced in the measurements by the particular antenna pattern of CIMR (mainly including the grating lobes) through the implementation of well-established image-processing techniques. The method shown is applied at image level, i.e., when the  $T_B$  measurements are recomposed to form a raster. The use of deconvolution techniques is motivated by two main mission requirements [10]:

- 1) impact of radiometric discontinuities (e.g., representative of a coastal boundary or sea ice edge) on L1B  $T_B$  measurements must be  $< \pm 0.5$  K at 1 footprint from a high contrast target scene transition (the radiometric difference ranges from 175 K at L-band to 115 K at Ka-band); and
- 2) L1 products must be available not later than 2 h after satellite measurement acquisition. The former requirement implicitly implies that CIMR L1B products should not have any land/sea or sea/ice contamination, thus the APC has to involve the observed scenario and cannot be fixed. The latter indicates the need for a computationally fast correction.

Although the correction is usually applied earlier in the processing chain (as devised for CIMR) the intent of the article is to demonstrate the concept. It should be noted that, although the study is based on CIMR characteristics and requirements, its applicability can be extended to other imaging radiometers.

The numerical deconvolution was applied to synthesized brightness temperatures. The latter are obtained by convolving the scenario defined in [10] (known as CIMR Test Card “Picaso v3.0” and referred to as TC) with the nominal antenna radiation-pattern assuming a push-broom acquisition. The CIMR TC is defined in [10] to be a stress-test for any candidate antenna-compensation algorithm. Despite being unrealistic, the number of sharp discontinuities and their number density in the space domain dramatically exert stress on the APC performance. The Picaso card helps in verifying the compliance with the CIMR accuracy requirements wrt to radiometric steep and/or gradient discontinuities; shape and orientation of the geometrical discontinuity with respect to the measurements; spatial radiometric variability of the scene under test.

To evaluate the performance of the APC technique, the map of the corrected  $T_B$ s was compared to the input TC.

TABLE I  
REQUIREMENTS AT ANTENNA LEVEL FOR THE HIGH-FREQUENCY CHANNELS  
OF THE CIMR MISSION

Channels	C	X	K	Ka
Center Frequency (GHz)	6.925	10.65	18.7	36.5
Maximum bandwidth (MHz)	650	100	200	1000
Polarization	V and H linear polarizations			
Footprint size (km)	≤ 15	100	≤ 5.5	< 5
Beam efficiency (%)	> 93			
Wide beam efficiency (%)	> 96			
Cross-polarization level (%)	< 2			
Total Standard Uncertainty (at 1 sigma) [K]	≤ 0.5	≤ 0.5	≤ 0.6	≤ 0.8

The rest of this article is organized as follows. Section II reports the description of the antenna system and the forward model for numerical evaluation of the observed temperature values. Section III resumes the impact of the grating lobes on the measurements of the scenario under test to introduce the methodology used to generate the expected  $T_B$  at footprint size scale and to explain the metrics used to evaluate the agreement with the mission requirements. The compensation algorithm is described in Section IV, whereas the numerical results are summarized in Section V. Comments and the perspective for future work are drawn in Section VI.

## II. ANTENNA SYSTEM AND FORWARD MODEL

### A. Antenna System

The CIMR instrument will observe the Earth in L-, C-, X-, K- and Ka-band at an average altitude of approximately 836 km with an observation zenith angle of  $55.0 \pm 1.5^\circ$ . For the C- to Ka-band channels, the antenna-level requirements that are relevant for this article are given in Table I. The analysis does not include the L-band as, at this frequency, the radiation pattern is almost a unique beam without any grating lobe looking towards the Earth. A requirement on the impact of grating lobes on  $T_B$  measurements when the instrument is close to discontinuities: it shall not exceed 0.5 K at one footprint from the border of the contrast target scene is fixed in [10].

The APC algorithm described in this article was applied to a mesh parabolic reflector with projected diameter  $D$  equal to 7.4 m, focal ratio  $f/D = 1$ , and clearance of 3.37 m. The mesh is defined by a pseudo-periodic triangular lattice with approximately 1000 nodes arranged in concentric rings [19]–[21].

The radiation pattern used in the article refers to a feed placed in the reflector focus and radiating an  $HE_{11}$ -like radiation-pattern [22].

Fig. 1 shows the normalized secondary-level radiation-patterns projected on ground corresponding to an angular region of  $[38, 55]$  deg (in the along-track direction)  $\times$   $[-10, 10]$  deg (in the across-track direction). The white rectangle indicates the on-ground region area of 400 km (in the along-track direction)  $\times$  260 km (in the across-track direction).

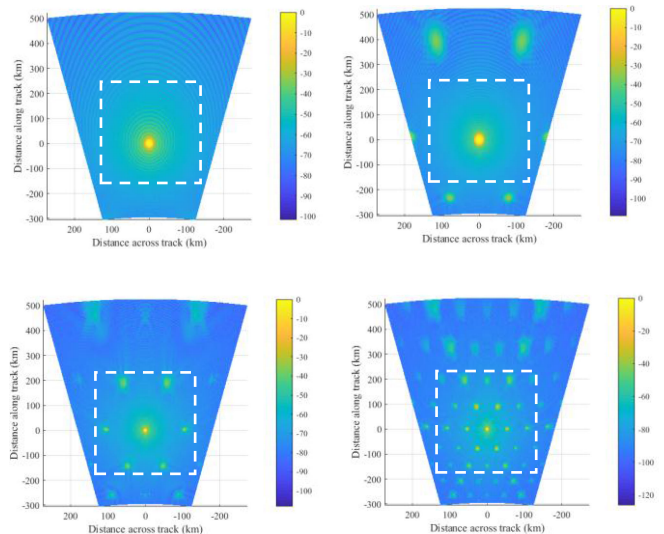


Fig. 1. On-ground projection of the normalized co-polar radiation patterns of the mesh-reflector antenna system considered in this article. From left to right: C-band channel; X-band channel (top panels); K-band channel; and Ka-band channel (bottom panels). The square rectangle indicates the on-ground area considered for the computation of the observed antenna temperatures.

This area has been considered in the computation of the measured antenna temperatures. At the lowest frequency C-band channel, this area is already  $26 \times 23$  footprints wide. As expected, Fig. 1 clearly points out that the grating lobes, represented by the quasi-circular region inside the portion of the antenna pattern stemming from the light blue background, are more evident, both in number and intensity, as the frequency increases. Focusing the attention on the areas delimited by a dashed white line that includes about 99% of the forward radiated energy, grating lobes effect is practically negligible at C- and X- bands (power level lower than  $-40$  and  $-36$  dB, respectively), whereas it is clearly visible at K- and Ka-band. In the latter case, of the 25 grating lobes populating this area, the closest 6 ones surrounding the main lobe bear a power level comprised between  $-30$  and  $-20$  dB with respect to the normalized maximum. It is worth also noticing the distance of the grating lobes from the main beam: they are able to collect appreciable energy up to hundreds of km away from the boresight.

The main features of the radiation patterns are given in Table II. The values refer to the feed antenna in the focus of the offset parabolic reflector.

### B. Forward Model

A simple forward model is used for computing the observed antenna temperatures,  $\bar{T}^{(\text{OBS})}$ . For a specific frequency channel, the observed antenna temperatures  $\bar{T}^{(\text{OBS})} = [T_H^{(\text{OBS})} T_V^{(\text{OBS})}]^T$  measured at the on-ground position  $\bar{\rho}_j$  by the two  $H$  and  $V$  linear-polarization channels of the radiometer can be numerically synthesized according to convolution product

$$\bar{T}^{(\text{OBS})}(\bar{\rho}_j) = \hat{\bar{G}}(\bar{\rho}) * \bar{T}_B(\bar{\rho})|_{\bar{\rho}=\bar{\rho}_j} \quad (1)$$

TABLE II  
MAIN FEATURES OF THE ANTENNA RADIATION-PATTERNS

Channels	C	X	K	Ka
Footprint size (km)	13.2	16.0	4.9	3.5
Ellipse major-axis (along track) (km)	17.0	20.7	6.2	4.4
Ellipse minor-axis (across track) (km)	9.8	11.7	3.6	2.6
Cross-polarization (%)	0.38	0.16	0.38	0.20
Beam efficiency (%)	97.1	99.4	96.5	96.8
Wide beam efficiency (%)	97.4	99.4	96.8	96.9
Grating-lobes level w.r.t. to main peak (dB)	< -40	< -36	< -31	< -24
Spill over (%)	1.7	0.3	1.8	0.7
On-ground power percentage outside the wide-beam region	0.6	0.1	1.2	2.2

where  $\bar{T}_B = [T_B^{(H)} \ T_B^{(V)}]^T$  is the vector of the brightness temperatures, and  $\hat{G}$  is the dyadic of the normalized gain coefficients

$$\hat{G}(\bar{\rho}) = \begin{bmatrix} \hat{g}^{(H,H)}(\bar{\rho}) & \hat{g}^{(H,V)}(\bar{\rho}) \\ \hat{g}^{(V,H)}(\bar{\rho}) & \hat{g}^{(V,V)}(\bar{\rho}) \end{bmatrix} \quad (2)$$

where  $\hat{g}^{(H,H)}(\bar{\rho})$  and  $\hat{g}^{(V,V)}(\bar{\rho})$  are the co-polar components of the radiation patterns, whereas  $\hat{g}^{(H,V)}(\bar{\rho})$  and  $\hat{g}^{(V,H)}(\bar{\rho})$  are the cross-polar terms. Since the meshing of the reflectors mainly affects the co-polar radiation patterns in terms of side and grating lobes, the APC developed in this article at first neglects the cross-polar contribution to (1) (i.e., the dyadic operator in (2) is diagonal)

$$\bar{T}^{(\text{OBS})}(\bar{\rho}_j) = \iint_{\Lambda} T_B(\bar{\rho}) \hat{g}(\bar{\rho} - \bar{\rho}_j) d\bar{\rho}. \quad (3)$$

The normalized radiation pattern  $\hat{g}(\bar{\rho})$  can refer either to the nominal antenna system as known after the pre-launch calibration campaign and the application of on-orbit model corrections or to the actual in-flight antenna-system affected by residual unknown uncertainties. The integration domain  $\Lambda$  corresponds to the considered on-ground coverage area of 400 km x 260 km. By discretizing the integration domain in regular pixels of limited dimension (e.g., 1 km x 1 km)  $\{\Lambda_j\}$  and assuming a uniform brightness temperature over each pixel, the vector  $\bar{T}^{(\text{OBS})}$  of the observed antenna temperatures can be computed through the vector convolution product

$$\bar{T}^{(\text{OBS})} = T_B * \hat{g} + \Delta \in \quad (4)$$

where  $T_B$  is the vector of the brightness temperatures  $\{T_{B,j}\}$ ,  $\hat{g}$  is the vector of the normalized-gain coefficients  $\{\hat{g}_j\}$  corresponding to each pixel, and  $\Delta \in$  is the vector of the discretization error. The elements  $\{\hat{g}_j\}$  of the latter vector are computed through a highly accurate Gaussian quadrature formula with nodes  $\{\rho_k\}$  and weights  $\{w_k\}$

$$\hat{g}_j = \iint_{\Lambda_j} \hat{g}(\rho) d\rho = \sum_k \hat{g}_{j,k} w_k. \quad (5)$$

For the Test Card which was tested here, the discretization in pixels of 1 km x 1 km introduces an error  $\Delta\varepsilon < 0.02$  K, thus being one order of magnitude smaller than the targeted value of 0.2 K for the antenna contribution to the Total Standard Uncertainty [10]. Once the observed antenna temperatures are computed over the dense 1 km x 1 km grid containing approximately 8.4 Mpixels, the data can be accurately interpolated to evaluate these temperatures in any position within a reference scenario.

### III. PERFORMANCE EVALUATION OF THE FORWARD MODEL

The brightness temperature  $T_B$  measured from space is commonly associated with the thermal emission radiated by the footprint area on the ground, which defines the spatial resolution of the instrument. In principle, this measurement can only be achieved by means of an ideal antenna whose radiation pattern is a step function coincident with the footprint. Indeed, any contribution coming from the region outside the footprint contaminates the measurements, introducing spurious information to the target  $T_B$ . This contamination can be a severe problem in the presence of grating and secondary lobes of appreciable intensity, as in the case of mesh reflectors under study (see radiation patterns in Fig. 1). These lobes provide contributions from areas that are far away, both in space and time, with respect to the main beam region. On the one hand, lobes looking forward with respect to the main beam “anticipate” the scene to be observed. On the contrary, those looking backward provide information from regions already scanned. The impact of the contamination depends on the radiometric contrast between the footprint  $T_B$  and the ones pertaining to regions illuminated mainly by the side and grating lobes. In this regard, the APC performances are tested over CIMR TC which is considered to be a representative scene for evaluating the performance of both the forward model and the APC.

In order to develop the APC algorithm for mesh reflectors and focus on the particulars of managing the compensation of several grating lobes, some simplifying assumptions have been made. This case study foresees one antenna-feed placed at the center of the focal plane that scans the TC mimicking a push broom acquisition over a Cartesian grid top-down from left to right.

To mimic CIMR acquisitions a continuous succession of gap-less nonoverlapped footprints grid, whose lattice steps coincide with the minor and major axes of the footprint ellipses given in Table II, was assumed without implications on the effectiveness of the APC algorithm performance. CIMR will perform measurements with an integration time such that one L1B measurement is obtained through combination—by weighted or linear averaging—of 5 samples to obtain 1 footprint almost gapless along scan and slightly overlapped along track. For sake of simplicity, the APC performance is tested assuming the measurements gap-less nonoverlapped. Hereinafter, this grid is referred to as “footprint-grid.” Since the footprints of the four channels are different, the corresponding data-sets are computed over different footprint-grids. These data sets are the inputs for the APC algorithm.

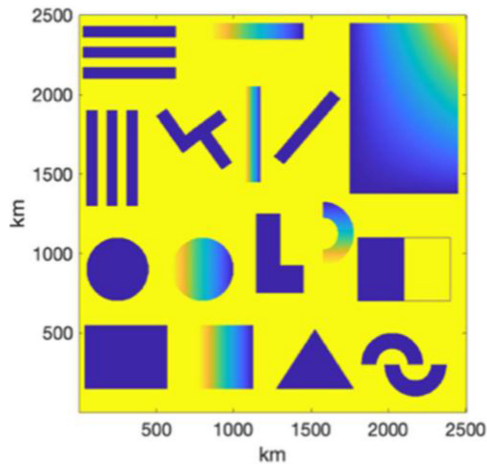


Fig. 2. CIMR TC. Shading shapes contain gradient variation, whereas the plain ones constant value. This structure is the same at all frequencies. Each shape is characterized by specific temperature value band dependent as given in Table III.

TABLE III  
BRIGHTNESS TEMPERATURE SPECIFICATIONS FOR THE TEST CARD OF FIG. 2

Channels	Higher $T_B$ (K)	Lower $T_B$ (K)	Constant $T_B$ (K)
C-band	250	75	75
X-band	250	80	80
K-band	250	100	100
Ka-band	250	135	135

#### A. CIMR Test Card “Picaso v3.0” (TC)

The ‘Picaso v3.0’ test card is the synthetic test scene suggested in [10] for the assessment of the radiometric performance of the CIMR instrument, including the impact of radiometric discontinuities. The TC is 2500 km  $\times$  2500 km wide and it has the same features for all the channels, except for the  $T_B$  values. Geometric discontinuities of variable shape, orientation, periodicity, and dimensions are embedded in a background set to a uniform temperature equal to 250 K (see Fig. 2). Discontinuities are characterized by brightness temperature features that exhibit either a constant value or gradients, both depending on the channel frequency, as given in Table III. The maximum and minimum  $T_B$  in columns two and three apply to all the discontinuities, whereas the rate of change is given by the shape size. The constant  $T_B$  values in plain shapes are listed in column 4. Uncertainty, when introduced, is assumed equal to  $\pm 2$  K at all frequencies for any shape and temperature feature. The effects caused by side and grating lobes generated by the mesh reflectors are observed at H pol for which the TC has been defined.

According to CIMR requirements, the performance is computed at a distance from any transition equal or greater than one footprint axis. To this purpose, for each channel a proper mask was defined in order to delimit the “do-not-care” region around the transitions where the radiometric performances should not be evaluated. It is worth underlining that the TC contains sharp

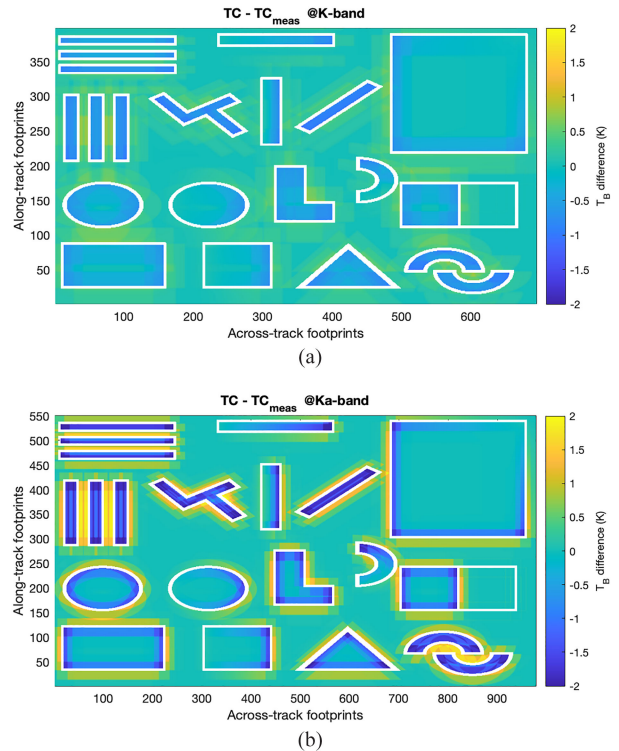


Fig. 3. Map of the temperature difference  $|\Delta T_B^{(OBS)}|$  between the numerically synthesized measurement  $T_B^{(OBS)}$  and the actual brightness temperature  $T_B$  over the test card. (a) K-band channel. (b) Ka-band channel. The white borders indicate the “do-no-care” regions in which the statistics are not computed.

transitions of high magnitude, representing, by far, worse cases than those occurring in actual data.

#### B. Observed Antenna Temperatures

The first step in the development of the present APC algorithm was to simulate the observed antenna temperatures for each frequency channel by convolving the antenna pattern with the scene. The convolution was performed for each node of the footprint raster. This operation simulates the measurement process performed with a real antenna. Then, the motion over the TC allows evaluation of the impact of the antenna pattern on the measured antenna temperatures. To this end, the difference  $\Delta T_B^{(OBS)}$  between the numerically synthesized measurement  $T_B^{(OBS)}$  and the actual brightness temperature  $T_B$  was computed over the entire TC for all the four channels. In order to evaluate the convolution (4) between the radiation pattern and the test card, the latter is padded with additional pixels at the background brightness temperature (250 K) to avoid issues on the borders of the scene. The percentage of the image satisfying the requirement  $|\Delta T_B^{(OBS)}| < 0.5$  K proved to be 99.9% for both the C- and X- channel, thus confirming that no APC algorithm is needed at these frequencies. On the contrary, the percentage decreases to 86.3% and 64.5% for the K- and Ka-band channels, respectively.

Fig. 3 shows the error  $|\Delta T_B^{(OBS)}|$  for the K- and Ka-band channels. As expected, the regions more affected by error are

those close to the boundaries of the radiometric transitions, where the error can be as high as 2 K. The blurring effect near the transitions depends on the radiometric contrast, the footprint size and the antenna pattern feature. At Ka-band [see Fig. 3(b)], these two factors jointly contribute to a wider contamination across the discontinuities. It must be underlined that these results do not depend on the TC orientation as almost identical results are obtained when it is brushed from left to right (or vice versa) or from top to bottom (or vice versa).

By following these analyses, we concluded that the APC was not needed at C- and X- band and the development of the APC algorithm was focused on the K- and Ka-band channels, only.

#### IV. ANTENNA PATTERN CORRECTION ALGORITHM

The devised APC algorithm is based on a regularized deconvolution of the measured data by exploiting the knowledge of the antenna pattern. It should be noted that the ground projection of the antenna pattern features (i.e., side and grating lobes) is known in finer detail than the coarse footprint grid. The size at ground of most of those secondary and unwanted lobes is comparable with the footprint size. To preserve most of the information in the convolution process, it has been chosen to interpolate the scene at the AP resolution rather than to down-sample the AP at the image resolution. To this end preprocessing and post-processing stages are inserted in the processing chain.

The APC preprocessing is devoted to sub-gridding the measurements at a finer resolution, i.e., from footprint size to  $1 \text{ km} \times 1 \text{ km}$ , as explained in Section II. Four interpolation methods were considered, namely: cubic spline, cubic convolution, linear and nearest neighborhood. The APC algorithm is independently applied to each polarization; thus, a generic polarization is considered in the following dissertation.

The pre-processing output, namely  $T_{\text{High-Res}}^{(\text{OBS})}$ , is the input of the regularized deconvolution stage, i.e., the kernel of the APC. This latter provides the estimation of the radiometric scene  $\hat{T}_B$  by minimizing its smoothness and bounding the reconstruction error, i.e., the error between the image to be reconstructed convolved with the antenna pattern and  $T_{\text{High-Res}}^{(\text{OBS})}$

$$\hat{T}_B = \arg \min_{T_B} \|\Delta T_B\|^2$$

provided that  $\left\| T_B \otimes \text{AP} - T_{\text{High-Res}}^{(\text{OBS})} \right\|^2 \leq \Delta$  (6a)

where  $\Delta$  is the Laplacian operator that accounts for the ‘‘roughness’’ of the image,  $\otimes$  is the discrete convolution operator and  $\Delta$  is the ‘‘accepted’’ reconstruction error energy. The value of  $\Delta$  is usually dictated by the impairments that affect the ideal convolution output. For instance, in the case of additive white Gaussian noise,  $\Delta$  corresponds to noise power. In the ideal case of no impairments,  $\Delta$  is usually set according to the desired numerical precision, in order to limit finite arithmetic effects.

The optimization problem in (6a) is convex but it is not in a suitable form to be solved. To this extent, it is preferable to

consider

$$T_B = \arg \min_{T_B} \left\| T_B \otimes \text{AP} - T_{\text{High-Res}}^{(\text{OBS})} \right\|_2^2 + \lambda \|T_B \otimes \Lambda\|_2^2$$
 (6b)

which is equivalent to (6a) for a suitable regularization weight  $\lambda$  that can be iteratively computed [23], [24]. Equation (6b) is also known as Tikhonov regularization or ridge regression and its solution can be derived in closed form.

The regularized deconvolution is performed in the frequency domain through the FFT to speed up the computation. This introduces some artifacts in the image under study whenever a sharp discontinuity is present (which frequently occurs in the CIMR TC case) known as ‘‘Gibbs effect’’ or ‘‘Gibbs ringing’’ and causes oscillations superimposed on the reconstructed image (a similar phenomenon is present also in SMOS  $T_B$  reconstructions, e.g., [24]). In order to cope with this effect, the solution is to low-pass filter the reconstructed image  $\hat{T}_B$  to limit the content of high frequencies. The cut-off frequency is the outcome of a tradeoff analysis between the need of filtering the ringing effects and the retaining of the intrinsic variability of the image. To do this, four families of 2-D windows were selected (Hamming, Blackman, Hanning, and Nuttall) [25] with several sizes (5 to 25 pixels, i.e., 5 to 25 km at 1 km spatial resolution).

The final step of the APC is the postprocessing, which consists of downscaling the estimated brightness temperature  $\hat{T}_B$  to the original footprint dimension, namely  $\hat{T}_B^{(\text{Low-Res})}$ . Finally, the performance of the APC algorithm is evaluated based on the following  $\Delta T_B$  metric

$$\Delta T_B = T_{\text{BTC}} - \hat{T}_B^{(\text{Low-Res})}$$
 (7)

where  $T_{\text{BTC}}$  is the initial TC value at footprint resolution and  $\hat{T}_B^{(\text{Low-Res})}$  is the output of the APC algorithm.

$\Delta T_B$  is evaluated both globally over the entire image ( $\Delta T_B^E$ ) and limited to the closest pixels to the transitions, but outside the 1-footprint regions ( $\Delta T_B^{1fp}$ ). The former provides a measure of the APC performance over the whole scene, whereas the latter focuses on the region close to the transitions, where artifacts and errors are more likely to occur.

#### V. APC NUMERICAL RESULTS

##### A. Tuning of APC Configuration

As outlined in the previous section, there are several options that must be set in the APC. These are considered one by one and their impact is computed in terms of the obtained  $\Delta T_B^E$  and/or  $\Delta T_B^{1fp}$  values (i.e., the best option is the one that provides lower values of the metric). The first considered option is the selection of the interpolation method for improving the resolution of the input image. To this end, different filtering after the regularized deconvolution have been applied. The best results were provided by the cubic spline interpolation with a  $\Delta T_B^E$  lower than 0.5K over the 98.4% of the TC values at Ka-band, and 92.2% at K-band. The worse results were shown by the nearest neighbor with 58.3% and 47.4% at Ka- and K-band, respectively. Hence, the cubic spline has been selected for the interpolation method

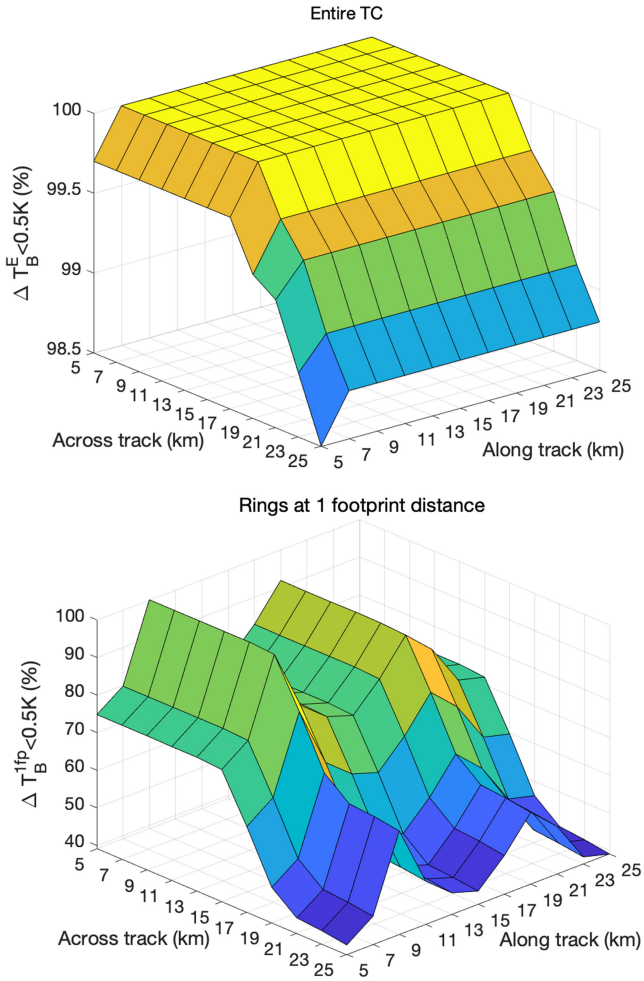


Fig. 4. Performance at Ka band of the APC with the Hanning window as a function of its size in across and along-track directions. (a) Best solution on the overall map and (b) in the region close to the transitions.

considering also the smoothness enforced by this technique that leads to lower Gibbs ringing with respect to the other methods. The second step in the APC tuning is the choice of the filter (window type and dimensions) that provides the best algorithm performance. The choice of the low pass filtering was heuristically driven by the effect on both  $\Delta T_B^E$  and  $\Delta T_B^{1fp}$  of jointly the type and size of the window.

The Hanning window has the best performance at the Ka-band as it meets the requirement for both  $\Delta T_B^E$  and  $\Delta T_B^{1fp}$  over the entire scene. By performing a similar analysis at K-band, it appears that the behavior of the chosen window is about the same, with a maximum fraction of 95.3% of the APC image meeting the  $\Delta T_B^E \leq 0.5$  K requirement. The fraction meeting the  $\Delta T_B^{1fp} \leq 0.5$  K requirement is slightly lower with value about 91%.

Fig. 4 depicts the fraction of TC satisfying the  $\leq 0.5$  K error when using the Hanning window, whose sizes are given in the reference plane. Considering the average performance  $\Delta T_B^E$  (top picture), any window whose size is greater than 7 km along-track and between 5 and 17 km across-track can be used. On the other hand, when considering  $\Delta T_B^{1fp}$  (bottom picture), the dimensions of the filtering window that provides the best

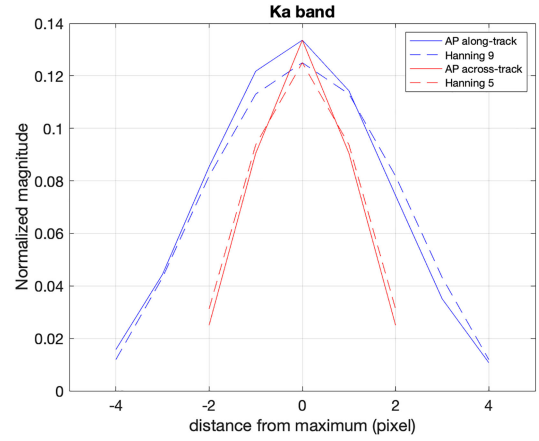


Fig. 5. Size of the optimal filtering window at Ka band.

results are equal to 9 km along-track and between 5 and 13 km across-track. Indeed, smaller windows are not able to mitigate the Gibbs ringing, whereas larger ones collect and mix the signal coming from the two sides of each transition.

Table IV gives the results of the filtering performance analysis at Ka-band. Blackman filter reaches almost the same score as the Hanning one but using a wider window. In Table V, the results of the filter performances are reported for K-band. Overall, the results are slightly worse than at Ka-band. Globally all the filters provide the same performance, with Hamming windows slightly over performing when the pixels close to the transitions are considered. About scores in Tables IV and V, it is worth pointing out that the number of pixels close to the transition that do not satisfy the  $\leq 0.5$  K requirement is so small that, globally, the metric could be rounded to 100%.

It is interesting to notice that the window that performs the better results has a shape similar to the one of the antenna pattern main beam, as shown in Fig. 5. This finding in some way recalls what is stated in [13], even if in that study the size close to the antenna beam is related to the best achievable spatial resolution.

The application of the APC algorithm enhances the quality of the measured scene towards meeting the requirement accuracy over the entire TC at Ka-band. The improvements are even more evident when looking at the statistics computed for the first rings of footprints surrounding the sharp transition, as reported in the fourth column of Table VI. Indeed, the best results are achieved by applying a regularized deconvolution with a Hanning window whose size is similar to that of the main beam.

The analysis carried out so far dealt with an ideal noiseless scene. Although being characterized by sharp transition of different shapes, the TC lacks the  $T_B$  variability typical of a natural homogeneous scenario. Thus, among the other performances, the APC algorithm has to prove robustness against small perturbations that are present in the scene. To this end, a white gaussian noise with zero mean and standard deviation  $s$  equal to 0.68 K was added to the TC, which corresponds to an uncertainty due to a Gaussian noise of about  $\pm 2$ K (the tails of the distribution were limited at these values). Noise signal is added to each single observation to mimic differences in the acquired scenes.

The APC-processed Ka- and K-band noisy scenes appear free from the grating lobes effect and maintain the TC features, i.e.,

TABLE IV  
RESULTS OF THE FILTERING PERFORMANCE ANALYSIS AT KA-BAND

Window	Fraction of TC meeting $\Delta T_B^E \leq 0.5K$	Size of the window (km)		Fraction of TC meeting $\Delta T_B^{1fp} \leq 0.5K$	Size of the window (km)	
		Along-track	Across-track		Along-track	Across-track
Hamming	99.9%	$\geq 7$	5÷15	96.1%	11	5÷13
Blackman	100%	$\geq 9$	5÷19	100%	13	7÷13
Hanning	100%	$\geq 7$	5÷17	100%	9	5÷13
Nuttal	100%	$\geq 11$	5÷21	97.3%	15	7÷19

TABLE V  
RESULTS OF THE FILTERING PERFORMANCE ANALYSIS AT K-BAND

Window	Fraction of TC meeting $\Delta T_B^E \leq 0.5K$	Size of the window (km)		Fraction of TC meeting $\Delta T_B^{1fp} \leq 0.5K$	Size of the window (km)	
		Along-track	Across-track		Along-track	Across-track
Hamming	95.3%	13	7÷17	91.3%	13	7÷13
Blackman	95.3%	17	9÷21	91.1%	15	9
Hanning	95.3%	13	5÷17	90.9%	11	7, 15
Nuttal	95.3%	19	9÷23	91.1%	19	11, 19

TABLE VI  
BEST RESULTS OF APC ANALYSIS

Fraction of TC meeting the requirement		$\Delta T_B^E \leq 0.5K$	$\Delta T_B^{1fp} \leq 0.5K$
Ka-band	Measurement	65%	21.1%
	Regularized Deconv only	98.4%	69.8%
	Reg. Deconv + Hanning 9x5	100%	100%
K-band	Measurement	87.5%	62.9%
	Regularized Deconv only	92.2%	41%
	Reg. Deconv + Hamming 13x7	95.3%	90.9%

at Ka-band the APC processed data show a Gaussian noise with  $-0.006$  K mean and  $\sigma$  equal to  $0.51$  K. At K-band the performance is similar, with a Gaussian noise in the corrected images having a mean value and a  $\sigma$  equal to  $-0.04$  and  $0.59$  K, respectively. The adoption of a regularization approach is stable and provides satisfactory results.

### B. Effects of the Antenna Pattern Uncertainty

Among the various effects to be considered when evaluating the APC algorithm performance operating in real-life conditions, one has to consider that the mesh of the physical antenna is known with a given limited accuracy due to the manufacturing processes and the method used to measure it. Actually, the actual position of the facet nodes, which determine the CIMR mesh reflector e.m. properties, may be affected by a nonnegligible uncertainty. Also, once deployed and pointed towards the Earth, they could possibly suffer from mechanical deformations and in

general present a shape not identical to the one measured on the ground. Thus, a sensitivity analysis was performed to evaluate the impact of these uncertainties on the APC accuracy.

The node position, whose geometry is briefly recalled in Section II-A, was perturbed considering 7 standard deviations  $\sigma_{nodes}$  values of the random process characterizing their distribution on the mesh ( $0.025, 0.050, 0.075, 0.1, 0.15, 0.2, 0.25$  mm). These values were chosen based on both the achievable mechanical precision of the reflector and the grating lobe reduction constraints [26], [27]. For each case, a total of 50 realizations of the perturbed antenna pattern were generated and convolved with the TC scenario to mimic the measurements with an actual antenna. Also, the APC algorithm was run using the ideal antenna pattern (i.e., the one known before the spacecraft launch). For each realization, the  $\Delta T_B$  is computed between the “measured” TC and the APC output. The standard deviation of  $\Delta T_B$  is computed over the 50 realizations by considering all pixels except the one footprint transition regions, in order to devise the average uncertainty introduced by an actual antenna in the measurement process and the magnitude of the APC correction. As expected, the mean error on observed  $T_B$  increases as the uncertainty on the node position increases. In addition, the error is concentrated close to the sharp transitions. The APC helps in lowering the impact of the nonidealities in the mesh reflector by correcting the spurious features of the antenna pattern. To quantify this improvement in Fig. 6, we plotted the global standard deviation of the error  $\Delta T_B$  as a function of the uncertainties on the mesh node positions. We chose the standard deviation since the mean  $T_B$  error is a fixed value that theoretically can be compensated. Fig. 6 highlights the fact that the APC test card with filtering



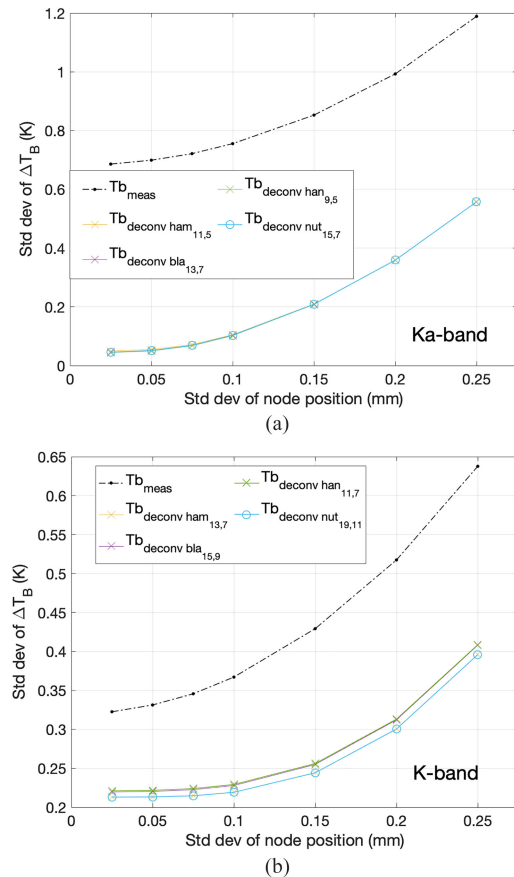


Fig. 6. Uncertainty introduced in the sensed scene by the measurement with an actual antenna (black dot-dashed), and the same after the APC processing.

(crosses and circles) usually performs better than the uncorrected measurements (black dash-dotted line) both at Ka- and K-band. For the highest channel, all the window kinds show similar results albeit with different sizes. At K-band, results are quite similar as in the previous case although the Nuttall window seems to perform slightly better. Overall, this analysis shows that the APC help in mitigating also the impact of uncertainties in the reflector characterization and that the standard deviation of the node position should be about 0.15 mm to fulfill the required performance with a reasonable margin.

## VI. CONCLUSION

The fulfillment of the future CIMR mission scientific requirements, in terms of spatial resolution and radiometric accuracy, can be attained with an unfurlable mesh reflector antenna that introduces as a major impairment the contamination of acquired measurements due to grating lobe contribution, especially at its high frequencies. This contamination must be removed via an APC algorithm to meet the tight radiometric requirement on measurement accuracy.

In this article, the authors have explored a numerical approach applied to synthetic scenarios based upon a test card designed [10] to reproduce steep and smooth variations in both spatial and thermal domains.

Basically, the algorithm performs a deconvolution of the antenna pattern on the synthetically measured values followed

by a low pass filtering. The goal of the APC algorithm is to reconstitute antenna temperature values with an error less than 0.5 K at a distance equal to the spatial resolution for each radiometric channel belonging to C-, X-, K-, and Ka-band.

The major conclusion is that, with the proposed and current reflector design, the channels that suffer the most from grating lobe contamination are those belonging to Ka- and K-band, whereas those belonging to X- and C- band show negligible or absent grating lobes and do not need to undergo an APC algorithm.

At Ka-band, the best performance of the APC is achieved by applying a regularized deconvolution with a Hanning window filtering sized 9 km × 5 km; in such a case, either over the entire TC or focusing on the region at 1-footprint distance from the transition, the requirement is fulfilled always, i.e., 100% of the observed antenna values has an error <0.5 K. At K-band, the same APC configuration meets the 0.5 K accuracy requirement over the 95.3% of the scene while the score is 90.9% at one footprint distance from the transitions. In addition, the APC proved to be reliable when applied either on noisy data obtained by adding white Gaussian noise with a standard deviation corresponding to an uncertainty of about ±2 K or to data measured with a perturbed configuration of the mesh reflector.

The uncertainties in the reflector geometry related to the mesh node deployment tolerances cause spurious measurements wrt the nominal antenna pattern. The APC applied to 50 realizations of the TC observed with a perturbed antenna pattern lowers the effect of these nonidealities. Namely, a  $\sigma_{nodes}$  of about 0.15 mm in node distribution results in a standard deviation in  $\Delta T_B$  - computed between the “ideally measured” TC and the APC output - of about 0.25 and 0.2 K, at K- and Ka band, respectively, instead of 0.43 and 0.85 K which would be obtained without APC.

Also, as CIMR mission will have a maximum latency (the time from the scene sensing and the availability of the L1B product to the users) of about 2 hours, it is mandatory that the APC algorithm introduces the slightest delay in the processing chain. The proposed APC was evaluated on a nondedicated machine (i.e., with several services running along with the APC): the personal computer featured an Intel Xeon CPU E3-1270 v6 with 64GB RAM and the MATLAB 2018b software ran under Microsoft Windows 10 operative system. The execution time resulted to be 11.8 sec and 11.4 sec at Ka- and K-band, respectively, for the APC of the TC.

Notwithstanding the results presented here cannot be considered as conclusive for CIMR, mainly because of the simplified scanning geometry, it can be concluded that the developed APC method is able to compensate the complex antenna pattern and in particular the grating lobes effect. The development of a complete analysis, which consider a real acquisition mode (i.e., multiple feeds and conical scanning) and a more realistic scenario is currently understudy. Results are expected to be available over the next year.

## ACKNOWLEDGMENT

The view expressed herein can in no way be taken to reflect the official opinion of the European Space Agency.

## REFERENCES

- [1] J. P. Hollinger, J. L. Peirce, and G. A. Poe, "SSM/I instrument evaluation," *IEEE Trans. Geosci. Remote Sens.*, vol. 28, no. 5, pp. 781–790, Sep. 1990, doi: [10.1109/36.58964](https://doi.org/10.1109/36.58964).
- [2] D. E. Barrick and C. T. Swift, "The seasat microwave instruments in historical perspective," *IEEE J. Ocean. Eng.*, vol. 5, no. 2, pp. 74–79, Apr. 1980, doi: [10.1109/JOE.1980.1145457](https://doi.org/10.1109/JOE.1980.1145457).
- [3] N. C. Grody and P. P. Pellegrino, "Synoptic-scale studies using the nimbus 6 scanning microwave spectrometer," *J. Appl. Meteorol.*, vol. 16, no. 8, pp. 816–826, Aug. 1977.
- [4] J. Simpson, C. Kummerow, W.-K. Tao, and R. F. Adler, "On the tropical rainfall measuring mission (TRMM)," *Meteorol. Atmos. Phys.*, vol. 60, pp. 19–36, Mar. 1996.
- [5] F. Karbou, C. Prigent, L. Eymard, and J. R. Pardo, "Microwave land emissivity calculations using AMSU measurements," *IEEE Trans. Geosci. Remote Sens.*, vol. 43, no. 5, pp. 948–959, May 2005, doi: [10.1109/TGRS.2004.837503](https://doi.org/10.1109/TGRS.2004.837503).
- [6] T. Maeda, Y. Taniguchi, and K. Imaoka, "GCOM-W1 AMSR2 level 1R product: Dataset of brightness temperature modified using the antenna pattern matching technique," *IEEE Trans. Geosci. Remote Sens.*, vol. 54, no. 2, pp. 770–782, Feb. 2016, doi: [10.1109/TGRS.2015.2465170](https://doi.org/10.1109/TGRS.2015.2465170).
- [7] P. Focardi, P. Brown, and Y. Rahmat-Samii, "A 6-m mesh reflector antenna for SMAP: Modelling the RF performance of a challenging Earth orbiting instrument," in *Proc. Int. Symp. Antennas Propag.*, 2011, pp. 2987–2990, doi: [10.1109/APS.2011.5997157](https://doi.org/10.1109/APS.2011.5997157).
- [8] K. D. McMullan *et al.*, "SMOS: The payload," *IEEE Trans. Geosci. Remote Sens.*, vol. 46, no. 3, pp. 594–605, Mar. 2008, doi: [10.1109/TGRS.2007.914809](https://doi.org/10.1109/TGRS.2007.914809).
- [9] E. P. Dinnat and D. M. Le Vine, "Effects of the antenna aperture on remote sensing of sea surface salinity at L-Band," *IEEE Trans. Geosci. Remote Sens.*, vol. 45, no. 7, pp. 2051–2060, Jul. 2007, doi: [10.1109/TGRS.2007.890807](https://doi.org/10.1109/TGRS.2007.890807).
- [10] *Copernicus Imaging Microwave Radiometer (CIMR), Mission Requirements Document*, Oct. 2020. [Online]. Available: <https://cimr.eu/sites/cimr.met.no/files/documents/>
- [11] E. G. Njoku, E. J. Christensen, and R. E. Cofield, "The seasat scanning multichannel microwave radiometer (SMMR): Antenna pattern corrections – development and implementation," *IEEE J. Ocean. Eng.*, vol. OE-5, no. 2, pp. 125–137, Apr. 1980, doi: [10.1109/JOE.1980.1145460](https://doi.org/10.1109/JOE.1980.1145460).
- [12] T. Mo, "AMSU-A antenna pattern corrections," *IEEE Trans. Geosci. Remote Sens.*, vol. 37, no. 1, pp. 103–112, Jan 1999, doi: [10.1109/36.739131](https://doi.org/10.1109/36.739131).
- [13] A. S. Milman, "Antenna pattern correction for the nimbus-7 SMMR," *IEEE Trans. Geosci. Remote Sens.*, vol. GE-24, no. 2, pp. 212–219, Mar. 1986, doi: [10.1109/TGRS.1986.289640](https://doi.org/10.1109/TGRS.1986.289640).
- [14] K. Teramoto, K. Arai, and T. Imatani, "Evaluation of the performance of antenna pattern correction under the influence of unknown antenna pattern changes," in *Proc. Int. Geosci. Remote Sens. Symp.*, 1993, pp. 1805–1807, doi: [10.1109/IGARSS.1993.322411](https://doi.org/10.1109/IGARSS.1993.322411).
- [15] K. Teramoto, K. Arai, and T. Imatani, "Antenna pattern correction for microwave radiometry utilizing a priori knowledge based on projection onto convex sets method," in *Proc. Int. Geosci. Remote Sens. Symp.*, 1995, pp. 1192–1194, doi: [10.1109/IGARSS.1995.521181](https://doi.org/10.1109/IGARSS.1995.521181).
- [16] C. T. Swift, M. A. Goodberlet, and S. C. Reising, "Antenna pattern synthesis and deconvolution of microwave radiometer imaging data," in *Proc. MicroRad*, 2006, pp. 216–221, doi: [10.1109/MICRAD.2006.1677092](https://doi.org/10.1109/MICRAD.2006.1677092).
- [17] J. Peng *et al.*, "Soil moisture active/passive (SMAP) l-band microwave radiometer post-launch calibration upgrade," *IEEE J. Sel. Topics Appl. Earth Observ. Remote Sens.*, vol. 12, no. 6, pp. 1647–1657, Jun. 2019, doi: [10.1109/JSTARS.2019.2902492](https://doi.org/10.1109/JSTARS.2019.2902492).
- [18] T. Meissner, F. Wentz, and D. Draper, "GMI calibration algorithm and analysis theoretical basis document, version G," *Remote Sens. Syst.*, 2012.
- [19] E. Medzmariashvili *et al.*, "New variant of the deployable ring-shaped space antenna reflector," *Space Commun.*, vol. 22, no. 1, pp. 41–48, 2009.
- [20] M. W. Thomson, "The astromesh deployable reflector," in *Proc. IEEE Antennas Propag. Soc. Int. Symp. Dig.*, 1999, pp. 1516–1519, doi: [10.1109/APS.1999.838231](https://doi.org/10.1109/APS.1999.838231).
- [21] H. Shi, S. Yuan, and B. Yang, "New methodology of surface mesh geometry design for deployable mesh reflectors," *J. Spacecraft Rockets*, vol. 55, no. 2, pp. 266–281, Mar. 2018, doi: [10.2514/1.A33867](https://doi.org/10.2514/1.A33867).
- [22] G. Addamo, O. A. Peverini, R. Tascone, G. Virone, P. Cecchini, and R. Orta, "A Ku-K dual-band compact circular corrugated horn for satellite communications," *IEEE Antennas Wireless Propag. Lett.*, vol. 8, pp. 1418–1421, 2009.
- [23] R. C. Gonzalez and R. E. Woods, *Digital Image Processing*, Hoboken, NJ, USA: Prentice-Hall, 2008.
- [24] V. González-Gambau, A. Turiel, E. Olmedo, J. Martínez, I. Corbella, and A. Camps, "Nodal sampling: A new image reconstruction algorithm for SMOS," *IEEE Trans. Geosci. Remote Sens.*, vol. 54, no. 4, pp. 2314–2328, Apr. 2016, doi: [10.1109/TGRS.2015.2499324](https://doi.org/10.1109/TGRS.2015.2499324).
- [25] J. G. Proakis and D. G. Manolakis, *Digital Signal Processing*, Upper Saddle River, NJ, USA: Pearsons, 2006.
- [26] C. Cappellin *et al.*, "Large mesh reflectors with improved pattern performances," in *Proc. 37th ESA Antenna Workshop Large Deployable Antennas*, 2016.
- [27] J. R. de Lasson, C. Cappellin, R. Jørgensen, L. Datashvili, and J. Angevain, "Advanced techniques for grating lobe reduction for large deployable mesh reflector antennas," in *Proc. IEEE Int. Sym. Antennas Propag USNC/URSI Nat. Radio Sci. Meeting*, 2017, pp. 993–994.



**Marco Brogioni** (Member, IEEE) was born in Siena, Italy, in 1976. He received the M.Sc. degree in telecommunications engineering from the University of Siena, Siena, Italy, in 2003, and the Ph.D. degree in remote sensing from the University of Pisa, Pisa, Italy, in 2008.

Since 2004, he has been with the Microwave Remote Sensing Group, Institute of Applied Physics Nello Carrara, Consiglio Nazionale delle Ricerche, Florence, Italy. From 2006 to 2007, he was a Visiting Student with the University of California at Santa

Barbara, Santa Barbara, CA, USA. He is also involved in the design and manufacturing of microwave radiometers (L- to Ka-bands). He is currently involved in several international projects regarding polar regions. His research interests include passive and active microwave remote sensing applied to snow by using satellite and ground-based data, especially regarding the development of electromagnetic models for passive and active microwave remote sensing of snow, vegetation, and soil.

Dr. Brogioni was the recipient of the Third Prize at the URSI GA Student Prize Paper Competition in Chicago, IL, USA, in 2008. He was the Chair of the 16th MicroRad 2020 virtual meeting and in the local organizing committee of the 10th MicroRad, Florence, in 2008 and the Microwave Signature Symposium of the URSI Commission-F, Florence, in 2010. He participated in the Italian Antarctic Expeditions, carrying out his research at Concordia Station (Dome-C) and Mario Zucchelli Station (Ross Sea) in 2013, 2015, and 2018.



**Ada Vittoria Bosisio** (Member, IEEE) received the M.S. degree in electronic engineering and the Ph.D. degree in applied electromagnetism from the Politecnico di Milano, Milano, Italy, in 1991 and 1995, respectively.

During her Doctorate degree, she was involved in the Olympus and Italsat propagation experiments for the aspects related to propagation-oriented radiometry (Ka band). From 1995 to 1997, she was a Research Associate with the CETP/CNRS Laboratory, Vélizy, France, where she has been active in measurements and analysis of forest attenuation and scattering at 2 and 6 GHz. From 1997 to 1998, she was with CNET/France Telecom, Issy Les Mx., France, as Ingenieur de Recherche, working on radio-wave effects induced by GSM on the environment and on individuals. From 1999 to 2001, she was with the Propagation Group, Politecnico, Milano, Italy, as a Research Associate working on satellite links at low elevation angle in K- and W-band and on propagation of TV broadcast and digital radio links over mountains through ray techniques. Since 2001, she has been a Researcher with Italian National Research Council, IEIIT Institute, Milano, Italy, working on remote sensing applications related to atmospheric science and tropospheric propagation. Her research interests include microwave radiometry and the interaction mechanisms between signal and complex media in the terrestrial biosphere.



**Alessandro Lapini** received the M.Sc. degree (summa cum laude) in telecommunications engineering and the Ph.D. degree in computer science, systems and telecommunications from the University of Florence, Florence, Italy, in 2010 and 2014, respectively.

Since 2014, he has been a Research Assistant with the University of Florence, where he was initially with the Department of Information Engineering and then with the Department of Industrial Engineering since 2015. From 2016 to 2018, he was a Research Fellow

with the Department of Industrial Engineering, University of Florence. Since 2019, he is with the Microwave Remote Sensing Group, Institute of Applied Physics Nello Carrara, Consiglio Nazionale delle Ricerche, Florence, Italy. His research interests include signal and image processing, particularly in the field of remote sensing and biomedical imaging, acoustics, and active noise control.



**Giovanni Macelloni** (Senior Member, IEEE) received the M.Sc. degree in electronic engineering from the University of Florence, Florence, Italy, in 1993.

Since 1995, he has been with Institute of Applied Physics-CNR-Florence, Florence, Italy, where is currently the Head of Research. Since 2019, he has been an Adjunct Professor with the University of Venice, Venice, Italy. He is also involved in the design and development of microwave remote sensing systems both from the ground, the air and satellites.

His research has been carried out in the framework of several national and international programs granted by Italian Entities, the European community and Space Agencies (ESA, ASI, NASA and JAXA) and includes the participation in international teams for the studying of the cryosphere and the development and assessment of future space-borne missions. His research interest includes microwave active and passive remote sensing for the study of the Earth System and cryosphere in particular.

Dr. Macelloni is a Member of the Cryonet team of Global Cryosphere Watch of the WMO, and of the Italian Scientific Antarctic Commission which implements the national Antarctic programme. He was a Tutor of Ph.D. students, was a Reviewer of several international committees, organizations and international journals, and acted as organizer and co-chair of international conferences. He is currently an Associate Editor of IEEE TRANSACTIONS ON GEOSCIENCE AND REMOTE SENSING.



**Giuseppe Addamo** (Member, IEEE) was born in Messina, Italy, in 1979. He received the Graduate degree with distinction (summa cum laude) in electronic engineering and the Ph.D. degree in electronic and communication engineering from the Politecnico di Torino, Turin, Italy, in 2003 and 2007, respectively.

In January 2007, he was a Research Fellow with the Istituto di Elettronica e di Ingegneria dell'Informazione e delle Telecomunicazioni, Consiglio Nazionale delle Ricerche, Turin, Italy, and in 2012, became a Researcher. He holds practical classes

in courses on electromagnetic field theory and mathematical analysis at the Politecnico di Torino. His research interests include microwave leaky antennas, dielectric radomes, high-power feed systems (e.g., orthomode transducers, microwave filters), corrugated horns, frequency-selective surfaces, and large dielectric radomes.



**Giuseppe Virone** (Senior Member, IEEE) Giuseppe Virone was born in Turin, Italy, in 1977. He received the Graduate degree with distinction (summa cum laude) in electronic engineering in November 2001 and the Ph.D. degree in electronics and communication engineering in 2006 from the Politecnico di Torino, Turin, Italy.

He is currently a Researcher with the Istituto di Elettronica e di Ingegneria Informatica e delle Telecomunicazioni, Italian National Research Council. He was with the IEIIT, as a Research Assistant in 2002.

He coordinated more than 15 scientific projects funded by both the industry and other scientific research organizations and joined more than 30 research projects as a collaborator. He authored 43 journal papers, 134 conference papers and Three European patents. His research interests include design, numerical analysis and characterization of microwave and millimeter waveguide passive components for feed systems, antenna arrays, frequency selective surfaces, compensated dielectric radomes and industrial sensing applications.



**Walter Di Nicolantonio** received the Master's degree in physics from the University 'La Sapienza' of Rome, Rome, Italy, in 1994.

He is currently with the Microwave Earth Observation Payload division of OHB Italia in Milan, Italy, designing algorithm specification for instrument simulators, ground processors and radiometric performance analysis. He was with the OHB Italia (former CGS) in 1998 working at CNR/ISAC—Institute of Atmospheric and Climate Sciences, Bologna, Italy—developing software for level s1 and 2 satellite data

processing. He developed and optimized algorithms for processing satellite data to retrieve optical properties of atmospheric aerosols and clouds. Up to 2015, he was in charge of the Bologna division of the OHB-I Earth Observation and Applications department working in national and international research projects in the field of satellite remote sensing of air quality. He is the author of 20 peer-reviewed journal articles and of more than 50 conference proceedings and technical reports in the fields of EO satellite remote sensing.



**Marco Grilli** was born in Milan, Italy, in 1973. He received the Graduate degree with distinction (summa cum laude) and the M.Sc. degree in electronic engineering from the Politecnico di Milano, Milan, Italy, in 1999.

He was with the OHB Italia (former Carlo Gavazzi Space, CGS), Milan, Italy, in 2000, working on the design of electronic boards for motor control and analog signals acquisition. Since then, he developed his skills in the field of system engineering and worked as system engineer and AIT manager on several Earth and

Space observation programs, including external payloads for the International Space Station (EuTEF, ASIM, Solar, SAGE III) and satellite missions (LARES, LISA). He is currently with the Microwave Earth Observation Payload division of OHB Italia, where he first worked on the development of the new MicroWave Imager, scanning radiometer for the MetOp-SG mission. Since 2018, he has been the CIMR Instrument System Engineering Manager, contributing to the definition of the system requirements, the feasibility study and now to the flight models development.



**Oscar A. Peverini** was born in Lisbon, Portugal, in April 1972. He received the Graduate degree (summa cum laude) with distinction in telecommunication engineering and the Ph. D. degree in electronic engineering from the Politecnico di Torino, Torino, Italy, in 1997 and 2001, respectively.

During his doctoral studies, he was a Visiting Researcher with the University of Paderborn, Paderborn, Germany, where he was involved in the design of acousto-optical devices. In 2001, he was a Research Fellow with the Department of Physics, Politecnico

di Torino, CNR-IRITI institute. In December 2001, he was with the CNR-IEIIT Institute, as a Permanent-Position Researcher. Since 2007, he has been a Senior Researcher with the CNR-IEIIT Institute. Since 2009, he has been the Responsible Coordinator of the CNR-IEIIT Applied Electromagnetics and Electronic Devices research unit. Since 2015, he has been a Research Associate with the Italian Space Agency. He has been the Technical Manager for several scientific programmes and industrial research contracts aimed at the development of microwave and millimeter-wave devices for space-borne applications. He was a Reviewer for several journals and conferences in the microwave area. He has authored and co-authored over 50 journal papers, 110 conference papers, and he is the co-inventor of Three European patents.

Dr. Peverini was the recipient of the 2005 CNR Award for Outstanding Research Achievements, the Best Italian Young Scientist Award on Electromagnetics in 2000 from the Italian Electromagnetic Society, and a Student Research Award from the IEEE-UFFC Society at the 2000 IEEE-UFFC Symposium. Since 2018, he has been the President of the Evaluation Board for the R&D projects submitted in the ICT area regarding the "Fund for Sustainable Growth" Programme of the Italian Ministry of Economic Development.